Astron. Astrophys. 341, 29–43 (1999)

ASTRONOMY AND ASTROPHYSICS

VLA observations of the giant radio galaxy 3C 449

L. Feretti[1], **R. Perley**[2], **G. Giovannini**[1,3], **and H. Andernach**[4]

[1] Istituto di Radioastronomia del CNR, Via P. Gobetti 101, I-40129 Bologna, Italy
[2] National Radio Astronomy Observatory, P.O. Box O, Socorro, NM 87801 0387, USA
[3] Dipartimento di Fisica, Universitá di Bologna, I-40100 Bologna, Italy
[4] Departamento de Astronomía, IFUG, Apartado Postal 144, Guanajuato, C.P. 36000, Mexico

Received 4 May 1998 / Accepted 25 September 1998

Abstract. In this paper we present multifrequency VLA observations of the giant radio galaxy 3C 449. High resolution and sensitivity data were obtained in total intensity and polarized flux at 1.365, 1.445, 1.465, 1.485, 4.685, 4.985 and 8.385 GHz.

The source is characterized by an unresolved core, two opposite symmetric jets, and very extended lobes. These new images show the source morphology in great detail, in particular we detect plumes and wiggles in the low brightness lobes. The source is considerably polarized at all frequencies. We find that the magnetic field orientation is parallel to the jet axis at the very beginning of the jet, and becomes perpendicular at about $10''$(5 kpc) from the core. In the low brightness regions, the magnetic field is circumferential to the edges of the emission region.

The spectral index map between 5 GHz and 8.4 GHz shows that the northern region beyond $1'$ from the core has a much flatter spectrum than the southern one.

We analyse the jet dynamics, and conclude that the jets are relativistic at the beginning, and decelerate significantly within $10''$(5 kpc) from the core.

We compute the rotation measure, using all seven frequencies between 1.4 and 8.4 GHz. We detect significant rotation measure with values within about $\pm$50 rad m^{-2} of the expected contribution of our Galaxy. The Faraday effect is likely to originate in an external screen, which is most probably the intergalactic medium of the group of galaxies around 3C 449. Moreover, we resolve the effect of the interstellar medium associated with the galaxy 3C 449 itself.

Key words: galaxies: individual: 3C 449 – galaxies: jets – galaxies: magnetic fields – radio continuum: galaxies

1. Introduction

The radio galaxies of luminosity lower than P_{178}=5$\times 10^{25}$ W/Hz, known as FR I objects (Fanaroff & Riley 1974) are often characterized by continuous two-sided jets running into large-scale lobe structures (plumes) which are edge-darkened (i.e with the brightness peak located less than halfway out from the nucleus) and whose steepest radio spectra lie in the outermost regions furthest from the host galaxy. The magnetic field in FR I jets is oriented predominantly along the jet at the beginning, becoming predominantly perpendicular to the jet further away from the core (Bridle & Perley 1984).

The observed morphologies of low-power jets have been used to argue that they are turbulent and propagating at sonic or transonic speed on the large scale (Bicknell 1984, Bicknell et al. 1990). On the other hand, recent observational work (Giovannini et al. 1995) leads to the scenario in which jets of low-luminosity radio galaxies are relativistic on parsec scales. This is consistent with unified models, where FR I radio galaxies form the parent population of BL Lac objects (Urry & Padovani 1995).

Parma et al. (1994) have examined the variation of jet sidedness ratio with distance from the core, total radio power and core prominence. Their results are consistent with the hypothesis that FR I jets slow down from $\beta \approx 0.6$ to sub-relativistic velocities on scales of 1 – 10 kiloparsecs, because of turbulent entrainment. Laing (1996) developed a two-component jet model consisting of a fast "spine" with perpendicular magnetic field, surrounded by a slower "shear layer", which interacts with the external medium. The "shear layer" has either parallel or two-dimensional magnetic field. Assuming that the jet is relativistic at the beginning and decelerates to non-relativistic speeds at large distances from the nucleus, net longitudinal or transverse apparent fields may result, as a consequence of relativistic aberration.

The symmetric twin-relativistic jet model is supported by several lines of evidence (see e.g. Laing et al. 1996), in particular the detection of superluminal motions. However, it is well established that some sources show components with subluminal motions, as it is the case e.g. for Centaurus A (Tingay et al. 1998), M 87 (Biretta 1996), Cyg A (Carilli et al. 1994). The subluminal jet components can be either interpreted as slow patterns on the relativistic flow, or due to non-relativistic nuclear ejection. The last possibility has been suggested by Sol et al. (1989), Pelletier & Roland (1989, 1990) and Pelletier & Sol (1992), who proposed the jet two-fluid model to explain the presence of compact structures moving at different speed in extragalactic jets.

Send offprint requests to: lferetti@ira.bo.cnr.it

Table 1. VLA Observing Log

Frequencies (MHz)	Band	A Date	A Time(h)	B Date	B Time(h)	C Date	C Time(h)	D Date	D Time(h)
1365/1445	L	APR94	1.5	APR93	5.1	JUL93	1.0	JAN94	0.6
1465/1485	L	APR94	1.6	APR93	5.1	JUL93	1.0	JAN94	0.5
4685/4985	C	MAR/APR94	0.8	APR93	5	JUL93	8.7	JAN94	1.8
8285/8485	X	MAR94	1	APR93	5.1	JUL93	5.5	JAN94	1.8

A typical radio galaxy of the FR I class is 3C 449, which is well known due to its very large angular size ($\sim 30'$). It is elongated in the NS direction and is characterized by long two-sided jets. It is relatively nearby (z=.0181), and therefore particularly suitable for a detailed study of the jet structure and of the polarization properties. Previous studies of this source at radio frequencies have been presented by many authors (see Andernach et al. 1992, and references therein). High resolution images were first presented by Perley et al. (1979), who studied the jet structure. The high symmetry of the 3C 449 jets has been taken as evidence for the radio source major axis lying close to the plane of the sky. The parent galaxy, UGC12064, is dumbbell and is the most prominent member of the Zwicky cluster 2231.2+3732. It shows a nuclear dust lane with a major axis diameter of $\sim 2''$ roughly in position angle 135° (Butcher et al. 1980). The optical isophotes show pronounced deviations from pure ellipses and gradients in ellipticity, which are clear indications of a strong gravitational interaction (De Juan et al. 1994, Balcells et al. 1995). Optical data obtained with the HST were presented by Capetti et al. (1994), who detected a 23 mag nucleus surrounded by a ring with a projected diameter of $0.4''$. The luminosity profile shows that the observed ring is actually the result of absorption. The size of this region is consistent with it being cold material associated with an extended accretion disk.

In this paper we present multifrequency VLA maps, at high resolution and sensitivity, which allow us to study the jet behaviour and the polarization. We use a Hubble constant H_0=50 km s^{-1} Mpc^{-1}, which implies a linear conversion to 0.52 kpc/arcsec at the distance of 3C 449.

2. Observations and data reduction

The data presented here were obtained with the Very Large Array (VLA) in all four configurations, at different frequencies in the L, C and X bands. The observing epochs and integration times are listed in Table 1. The source 3C286 was used as a primary flux density calibrator. The phase calibrator was the nearby point source 2200+420, observed at intervals of about 20 minutes, while the calibrators for the polarization position angle were 3C138 and 3C48. The on-axis instrumental polarization of the antennas was corrected using the secondary calibrator 2200+420, which was observed over a wide range of parallactic angles. The data were reduced with the Astronomical Image Processing System (AIPS), following the standard procedure: Fourier-Transform, Clean and Restore. Self-calibration was applied to minimise the effects of amplitude and phase uncertainties. The X-band data obtained at 8285 GHz and 8485 GHz were averaged. The data-sets from different configurations were first reduced separately, each undergoing several iterations of cleaning and phase self-calibration. At 8.4 GHz and 5 GHz, the unresolved radio nucleus was subtracted in each individual data-set to avoid undesirable effects of core flux variability in the final maps. Table 2 lists the core flux densities subtracted at each frequency and epoch. To produce the merged data at each frequency, the D and C data-sets were concatenated first, then the B data-set, and finally the A data-set were added. At each step the data-sets were self-calibrated to ensure phase consistency.

Table 2. Core flux densities

Date	Conf.	$S_{5\,GHz}$ mJy	$S_{8.4\,GHz}$ mJy
APR93	B	31.0	40.7
JUL93	C	37.0	45.0
JAN94	D	36.0	45.0
MAR94	A	37.6	43.4
APR94	A	38.7	–

At each of the seven frequencies, maps of the Stokes parameters I, Q and U were produced with three different resolutions, using the AIPS task IMAGR. The restoring beam was a circularly symmetrical Gaussian, with FWHM = $1.25''$, $2.5''$ and $5''$. The images with the highest resolution at 8.4 GHz ($0.5''$ and $0.8''$) and 4.9 GHz ($0.8''$) were produced by applying the Maximum Entropy Method (task VTESS), to ensure the proper imaging of resolved low-brightness structure. The images of the polarized intensity were obtained as $P = (Q^2 + U^2)^{1/2}$, and corrected for the positive Ricean bias due to this combination of two noisy quantities in quadrature (Wardle & Kronberg 1974). The polarization angle was derived according to $\theta = 0.5 \tan^{-1}(U/Q)$.

3. Results

3.1. Total intensity images

The overall source structure is easily visible at 1.4 GHz, at a resolution of $5''$ (Fig. 1). The source is characterized by an unresolved core, two opposite symmetric jets, extending for $\sim 1'$ from the core, and the lobes of lower brightness. The total extent of the source mapped at this frequency with the VLA is about $20'$, which is slightly smaller than the extent found from single dish images (Andernach et al. 1992). In Fig. 1 some rel-

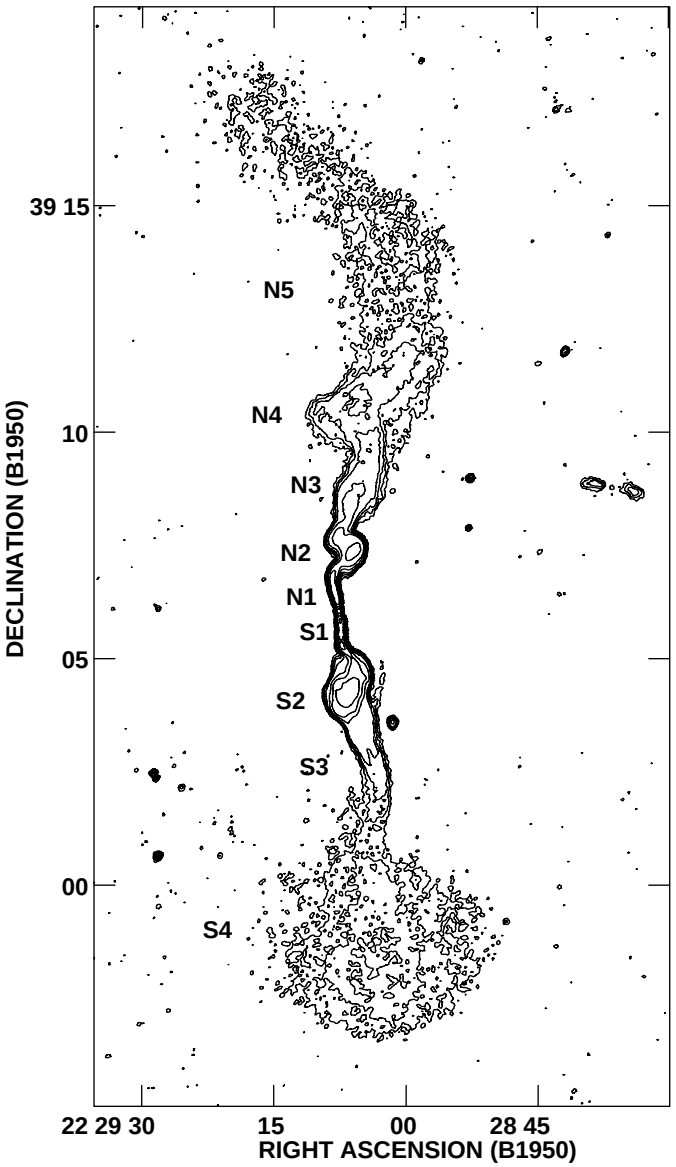

Fig. 1. Contour map of 3C 449 at 1.365 GHz with $5''$ angular resolution. Contour levels are 0.1, 0.25, 0.5, 1, 2.5, 5, 10, 25, 50, and 100 mJy/beam. The rms noise level in the map is 0.035 mJy/beam.

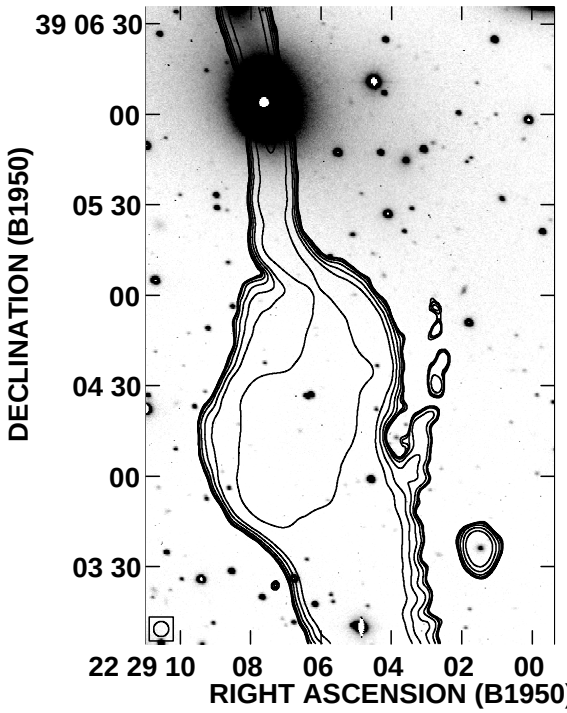

Fig. 2. 1.4 GHz radio contours of the region of the arc-like feature are superposed onto an I-band 15 min CCD image taken at the UH $88''$ telescope.

evant source regions are labelled for further reference. The two innermost jets (N1 and S1) seem fairly symmetrical at this relatively low resolution, although they are not perfectly opposite to each other. They are misaligned by $\sim 11°$, as mentioned by Perley et al. (1979). They both merge at about the same distance from the core into prominent inner lobes of high brightness (N2 and S2), different in structure. On larger scales, beyond the inner lobes N2 and S2, the source is rather asymmetrical. In the northern part the structure widens (region N3), then bends to the east into region N4, at which point there is a sharp bend of 90° bend to NW. The eastern boundary of region N4 resembles the corner of a square. Further out, the structure (N5) is first oriented in the NS direction, and then bent in a far trail toward NE. This region has a very low brightness, and smoothly fades into the noise. In the southern part, the structure emerging from the inner lobe S2 and directed toward SW (region S3) seems to be a channel with edge brightening, and becomes narrower at increasing distance from the core. Further to the south this streamer merges into a large, almost round lobe of very low brightness (S4).

The overall low-brightness structure is characterized by wiggles, filaments and plumes. There is a remarkable, faint, arc-like feature, westward of the southern lobe S2. It is actually detached from the lobe and it is very unusual. An I-band CCD image of this region was obtained with the 88-inch telescope of the University of Hawaii (see Fig. 2), and no object clearly responsible for this emission has been found. Therefore, we believe this structure to be associated with 3C 449.

In the field mapped at 1.4 GHz, there is an extended unrelated source at RA(B1950)=$22^h\ 28^m\ 36.5^s$, DEC(B1950)= $39°\ 08'\ 47.7''$, which shows a double-lobed structure, with a total flux of 12.5 mJy. It has no optical counterpart in the R plate of the Palomar Digitized Sky Survey, and must surely be an unrelated background radio galaxy.

At higher resolution (Fig. 3), 3C 449 is detected only in the innermost $8'$, with great structural details. The jets show some level of asymmetry in brightness, but they are very similar in transverse size. The two jets are not straight, but show a gradual curvature to the east. This behaviour is responsible for the misalignment of the two jets detected at lower resolution. At approximately $\sim 45''$ north and south of the core, the two jets show a prominent bend westward. After the bend, the northern jet widens and forms the higher brightness inner lobe (N2 in Fig. 1), which has a sharp and round edge on its NW boundary.

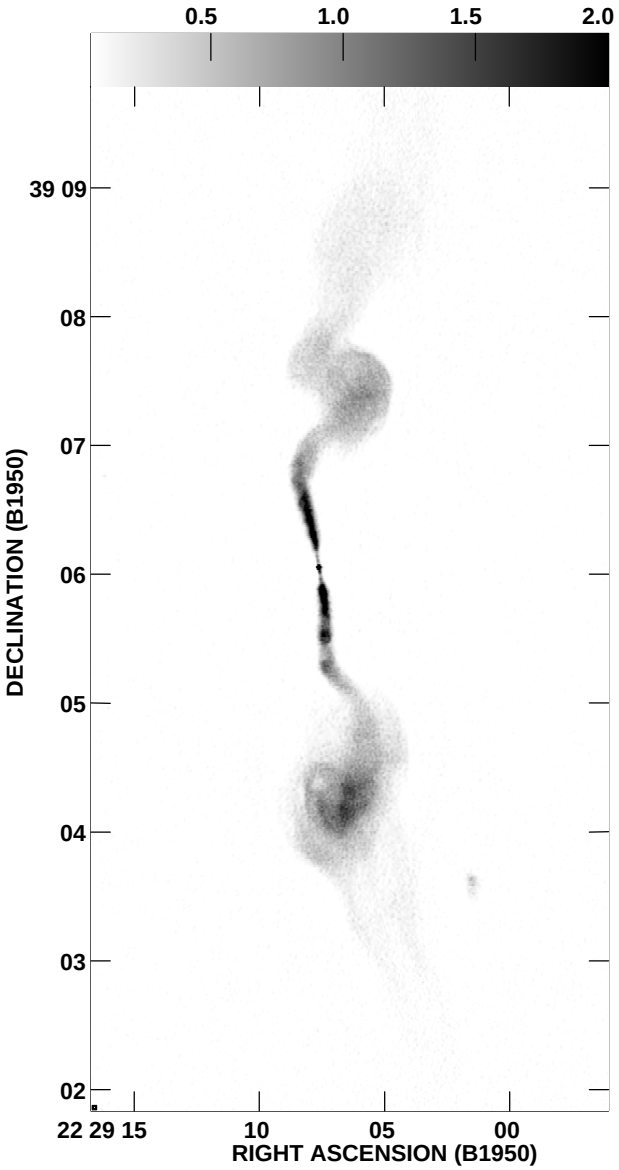

Fig. 3. Grey scale image at 1.365 GHz with 1.25″ angular resolution. The grey scale range is 0.05 to 2 mJy/beam. The rms noise level in the map is 0.031 mJy/beam.

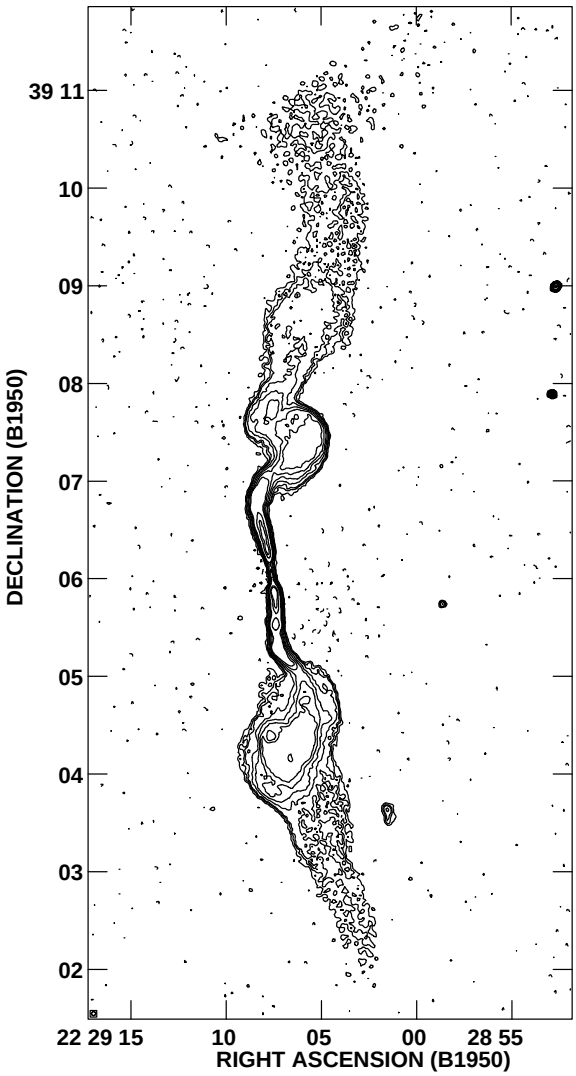

Fig. 4. Image of the source at 4.985 GHz with 2.5″ angular resolution. The unresolved radio core has been subtracted. Contour levels are -0.05, 0.05, 0.1, 0.15, 0.3, 0.5, 0.75, 1, 2.5, and 3.5 mJy/beam. The rms noise level in the map is 0.018 mJy/beam.

From there the streamer continues due NE and narrows at the same time up to a well-defined leading edge, before it sharply bends toward NW again. The whole structure is reminiscent of a helix. The southern jet at 45″ from the core has a sharper westward bend than the northern jet, and seems more collimated even after the bend. After a smooth bend along a long arch towards E, it forms the bright inner lobe (S2 in Fig. 1) which has a higher brightness than the corresponding northern one. The jet can still be distinguished within the lobe, where it follows a curved trajectory. Also noticeable is a loop emerging from the eastern side of the S2 lobe, suggesting a helical motion. The channel in the region S3 clearly exhibits enhanced emission at the edges. The western edge seems to be the continuation of the north-eastern loop, while the eastern one emerges from the lower brightness southern part of the lobe. We are possibly seeing two source regions in projection along the line of sight.

The features detected at 1.4 GHz are easily visible in the maps at high frequencies, where the nucleus has been subtracted because of its small, but noticeable variability (see flux densities in Table 2). Fig. 4 gives the image at 5 GHz, where the source is detected over a total extent of ∼8′. The details are strikingly similar to those at lower frequencies, with filaments and plumes.

The maps at highest resolution are those where the jets are heavily resolved. Figs. 5 and 6 present the images at 8.4 GHz with resolutions of 0.8″ and 0.5″, respectively, obtained with the Maximum Entropy Method. These maps clearly show the structure of the jets, which are exactly aligned only within 10″-12″ from the core, with a position angle of ∼9°. The position angles of the northern and southern jet on a larger scale are ∼13° and ∼182°, respectively. In Fig. 5, the radio image is

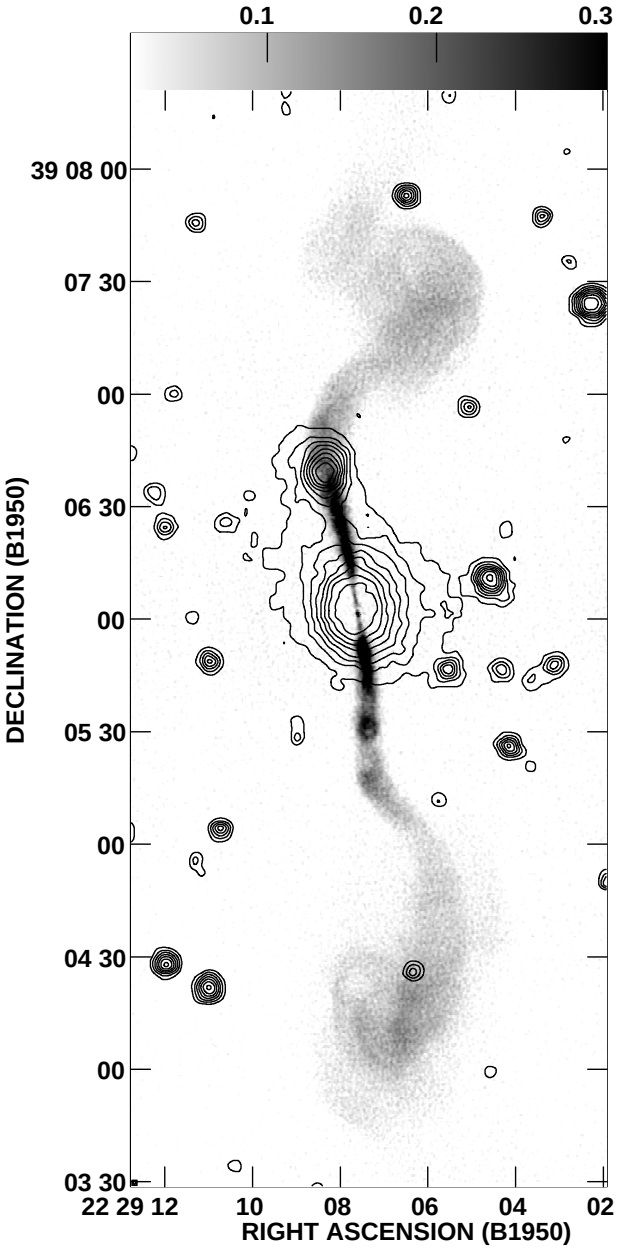

Fig. 5. Grey scale image of the source at 8.4 GHz with 0.8″ resolution, overlayed onto the optical image from the red Palomar Digitized Sky Survey. The unresolved radio core has been subtracted. The grey scale range is 0.02 to 0.3 mJy/beam. The rms noise level in the map is 0.011 mJy/beam.

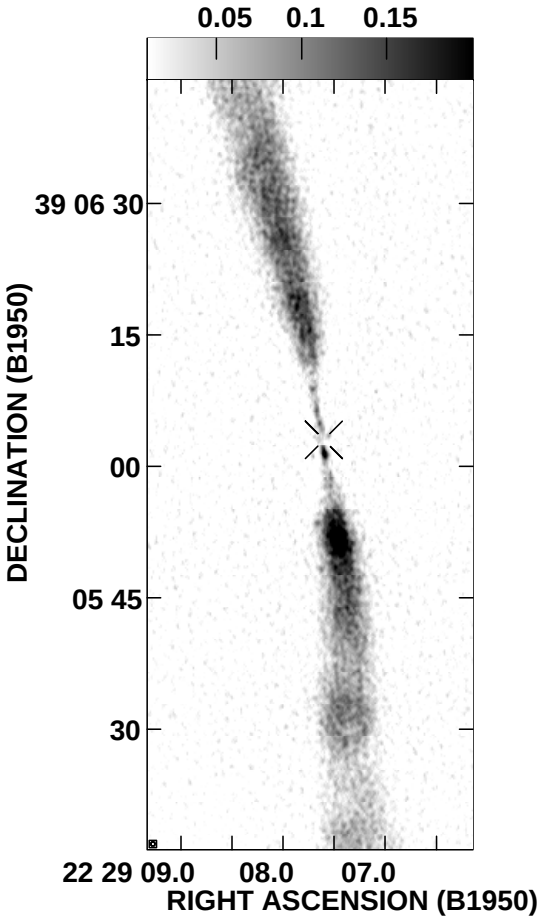

Fig. 6. Grey scale image of the innermost jets at 8.4 GHz, at the highest available angular resolution of 0.5″. The unresolved core has been subtracted at the position marked by a gapped X sign. The grey scale range is 0.01 to 0.2 mJy/beam. The rms noise level in the map is 0.011 mJy/beam.

overlaid onto the optical image from the Digitized Palomar Sky Survey. The ring of absorbing material (dust lane), as found by Butcher et al. (1980), is not visible here. It is easily visible in the image available in the public archive of the Hubble Space Telescope, and is located toward SW, roughly in position angle 135° and is therefore not perpendicular to the jets, as found in other FR I radio galaxies (Capetti & Celotti 1998).

Some degree of asymmetry between the two jets is evident, with the southern jet being slightly brighter on average than the northern one. The two jets are of very low brightness at their beginning, and no gap of radio emission is found close to the nucleus. At ∼2″ from the core, the southern jet shows a brightening, which has no similar counterpart in the opposite jet. Both jets suddenly flare and widen, at about 8″ from the core. The brightness of the southern jet shows a distinct maximum at ∼10″, followed first by a decrease in brightness, and then by a transverse structure similar to a bow-shock at ∼35″ from the core. In the northern jet, the trend of brightness is smoother. The jets are easily distinguishable for about 1′, where they merge into the inner lobes.

3.2. Spectrum

The spectrum of 3C 449 between 330, 1445, and 4835 MHz, with 3.6″ resolution, has been analyzed in detail by Katz-Stone & Rudnick (1997, hereinafter KR). Here, we obtained the map of spectral index between 4.985 GHz and 8.4 GHz with 2.5″ resolution (see Fig. 7). The spectrum is constant along the two jets, including the bends at ∼45″ from the core, with an average spectral index $\alpha_5^{8.4}$ = 0.58±0.03 ($S_\nu \propto \nu^{-\alpha}$). In the northern inner lobe (N2), beyond the bend of the jet, the spectrum index

is still rather flat, with an average value of 0.57±0.03, and becomes even flatter at the NW boundary. In the southern inner lobe (S2), the spectrum is much steeper than in the jet. In the center and southern edge of the lobe, where the jet is still traceable either from the high resolution images and from the polarization behaviour, the spectral index is 0.74±0.03, while on both sides it increases up to ∼0.9. There is therefore a remarkable asymmetry in the spectral behaviour between the northern and southern regions: the spectrum of the northern inner lobe is as flat as that of the jet, while the southern one is characterized by a significant steepening.

3.3. Polarization

The source is considerably polarized at all frequencies. Fig. 8 presents the 8.4 GHz map, with the magnetic field vectors superimposed (corrected for RM, see next subsection). The orientation of the magnetic field is longitudinal at the very beginning of the jet, where the polarization percentage is lower, and becomes transversal at larger distance from the core, and in the bending regions at ∼45″ from the core. In the SW part of the lobe N2 the magnetic field is transversal to the main ridge of emission, while in the NE part of the northern inner lobe N2, after the bend of the structure by 90°, the magnetic field is oriented along the main ridge of emission. In the southern inner lobe (S2) the magnetic field is transversal over most of the lobe, confirming that this is the continuation of the jet, but it is circumferential to the structure in the southernmost edge of lobe S2.

The polarization percentage at 8.4 GHz (Fig. 9) is somewhat patchy, and shows similar behaviour in the northern and southern source regions. In the innermost weak jets within few arcsec from the core, the degree of polarization is around 15% on both sides. Further out, the jet polarization percentage increases to about 30%, then it drops to 15-20% in the bends. In the inner lobes N2 and S2, the values of the degree of polarization are 30-50%. The map of the polarization percentage enhances the structures detected in total intensity: in particular the bow structure in the southern jet (∼32″ from the core) is prominent for its high fractional polarization and a similar feature is now discernable in the northern jet. Also, the loop in the southern inner lobe is very well seen in the polarization percentage map and a similar loop is found at the northern boundary of the northern inner lobe. We note that the polarization percentage is fairly constant transverse to the jet. Only the NW edge of the inner lobe N2 shows enhancement.

The source is not significantly depolarized at 4.985 and 4.685 GHz. At the lower frequencies, around 1.4 GHz, the average polarization percentage is about 0.75-0.8 of that at 8.4 GHz in the jets, while in the inner lobes (N2 and S2) no significant depolarization is found. It is worth noting that polarized brightness at the level of 30-40% is also detected in the large scale structure (Fig. 10), which is not imaged at higher frequencies because of its low brightness and missing short spacings. We also note that the two bright edges of the channel in the region S3 (see Fig. 1) are well separated because of their high degree of polarization and a similar feature of two parallel polarized streamers is found to emerge northward from the inner lobe N2.

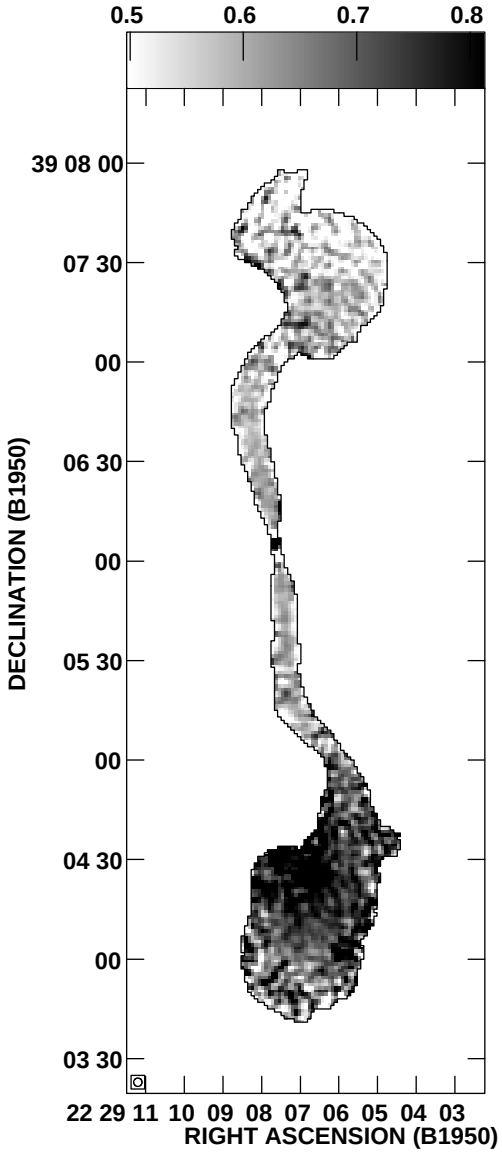

Fig. 7. Map of the spectral index between 4.985 GHz and 8.4 GHz, with 2.5″ resolution. The core has been subtracted. The contour is drawn at the level of 0.4.

3.4. Rotation measure

We obtained an image of the rotation measure (RM), by combining the maps of the polarization **E** vector at the seven frequencies available to us. We used the maps with all available resolutions (1.25″, 2.5″, and 5″), after blanking the pixels where the uncertainty in the polarization angle exceeded 20°. Following the definition $\theta_\lambda = RM\lambda^2$, where θ_λ is the position angle of the polarization vector at the wavelength λ, the value of the RM at each valid pixel was computed by linear fitting of the polarization angle as a function of λ^2. The fitting algorithm provides a

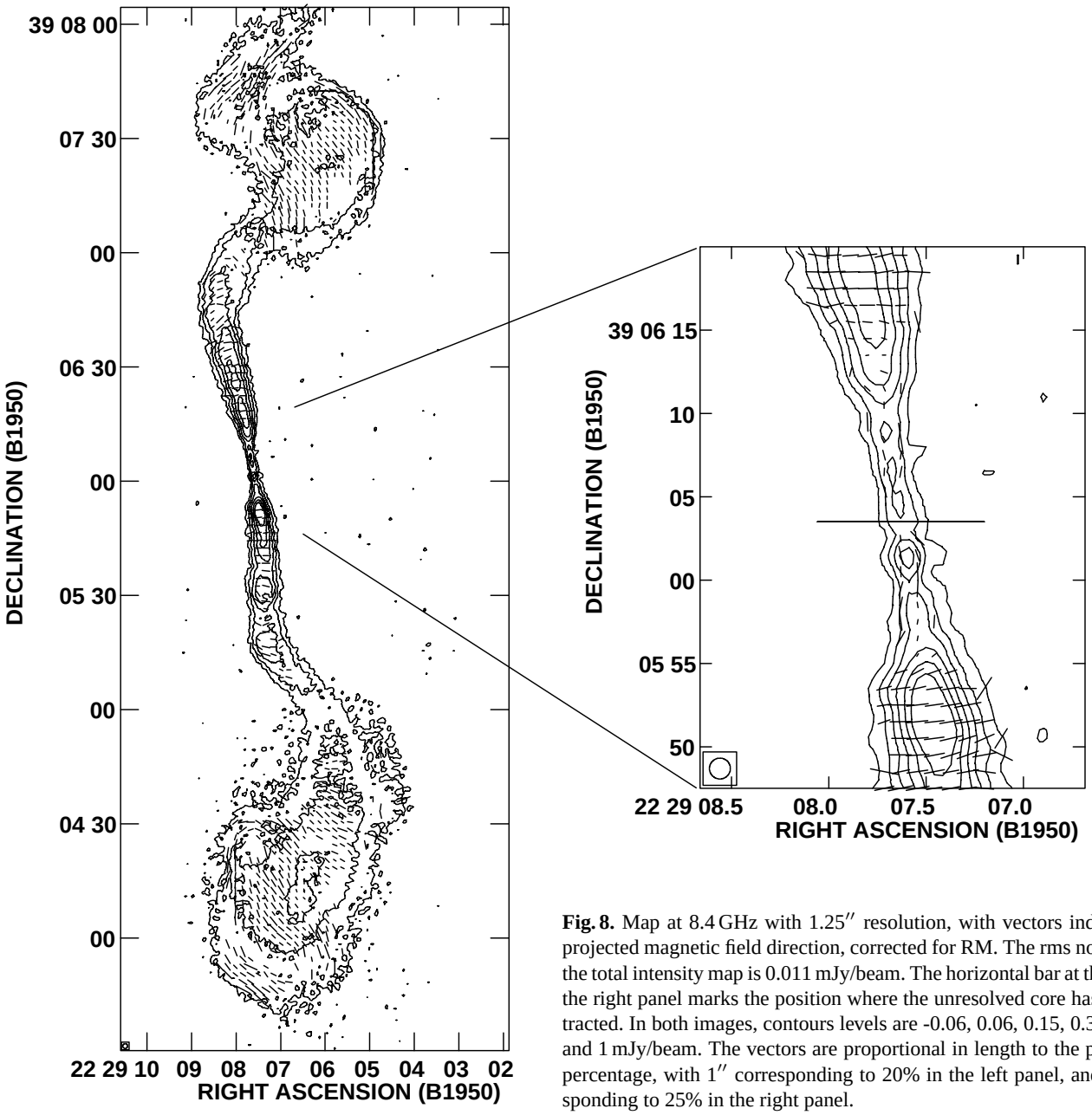

Fig. 8. Map at 8.4 GHz with 1.25″ resolution, with vectors indicating the projected magnetic field direction, corrected for RM. The rms noise level in the total intensity map is 0.011 mJy/beam. The horizontal bar at the center of the right panel marks the position where the unresolved core has been subtracted. In both images, contours levels are -0.06, 0.06, 0.15, 0.3, 0.5, 0.75, and 1 mJy/beam. The vectors are proportional in length to the polarization percentage, with 1″ corresponding to 20% in the left panel, and 1″ corresponding to 25% in the right panel.

weighted least-squares fit, allowing for an ambiguity of $\pm n\pi$ in each polarization position angle.

The data are well fitted by a λ^2 relation, as shown by some sample fits plotted in Fig. 11. The formal errors on the best-fit results are typically less than 2 rad m^{-2}. The values of RM range between -210 and -100 rad m^{-2} (see histogram in Fig. 12), with a peak around -162 rad m^{-2}, which corresponds to the expected foreground RM of our Galaxy (Andernach et al. 1992). The distribution of the RM is non-gaussian, with an excess of more negative values with respect to the average. The map of RM with the highest angular resolution (1.25″) is given in Fig. 13. A remarkable feature in the RM map is the large symmetry in the inner jets, within $\sim$15″ from the core, where the mean RM is more negative than the Galactic value (<RM> = –198 $\pm$ 3 rad m^{-2}).

At larger distance from the core, the RM in both jets flips to values more positive than the Galactic value and a clear asymmetry between the two jets becomes most evident in the bends. In the northern jet, there is some transversal structure and the values of RM change from –146 $\pm$ 10 rad m^{-2} to –185 $\pm$ 6 rad m^{-2} in the bending region. In the southern jet, the values of RM are always more positive than the Galactic value, from –152 $\pm$ 5 to –116 $\pm$ 5 immediately before the bending, and –138 $\pm$ 5 rad m^{-2} in the bending region.

The two inner lobes N2 and S2 are quite similar, with the average RM close to the Galactic value. The maps of the RM obtained with lower resolution are in excellent agreement with

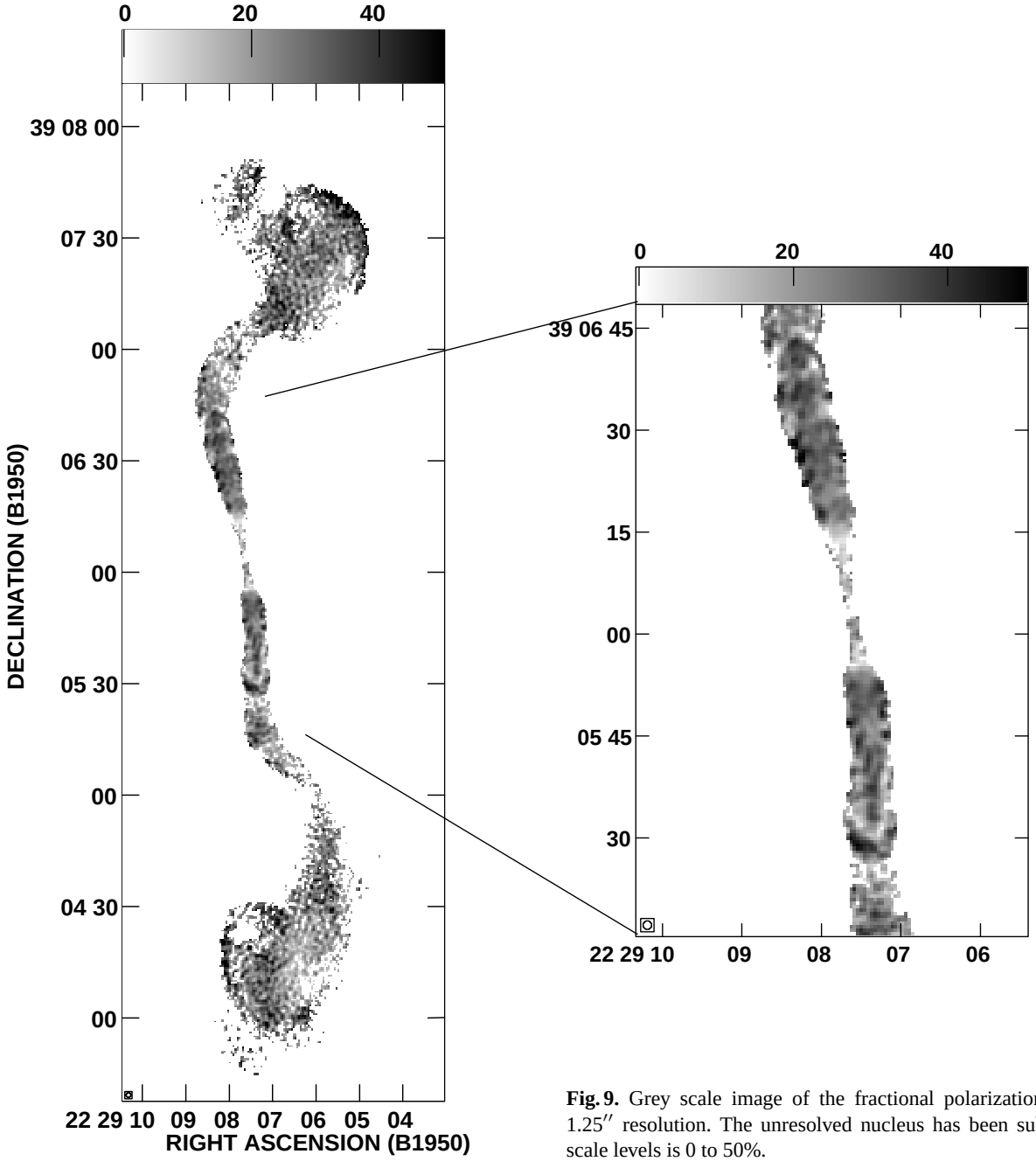

Fig. 9. Grey scale image of the fractional polarization at 8.4 GHz with $1.25''$ resolution. The unresolved nucleus has been subtracted. The grey scale levels is 0 to 50%.

the map at $1.25''$ resolution, indicating that the fluctuations of RM are resolved. Variations of the RM occur on similar scales in the jets and lobes, with typical size of $\gtrsim 10''$, i.e about 5 kpc.

4. Discussion

4.1. Jet collimation

We used the 8.4 GHz maps with $0.5''$ resolution to derive brightness profiles perpendicular to the jet axes. These were fitted with a Gaussian function to obtain the FWHM Φ_{obs} and peak surface brightness I_{obs} of the jets at various distances from the radio core. In order to derive intrinsic quantities, these parameters were deconvolved of the CLEAN beam Φ_{beam}, with the following formulae (Killeen et al. 1986):

$$\Phi = (\Phi^2_{obs} - \Phi^2_{beam})^{1/2} \quad (1)$$

$$I_\nu = I_{obs}(1 + \Phi^2_{beam}\Phi^{-2})^{1/2} \quad (2)$$

These parameters are plotted in Fig. 14, where the dots and open circles refer to the southern and northern jet, respectively. The two jets show very similar behaviours in the collimation properties, which can be divided into three regimes: an opening angle of $\sim$8.5° at the jet beginning, a rapid expansion between $6''$ (3 kpc) and $10''$ (5 kpc) from the core, with an opening angle of $\sim$17°, and finally a recollimation beyond $10''$, with an opening angle of $\sim$7.5°. The rapid expansion coincides with

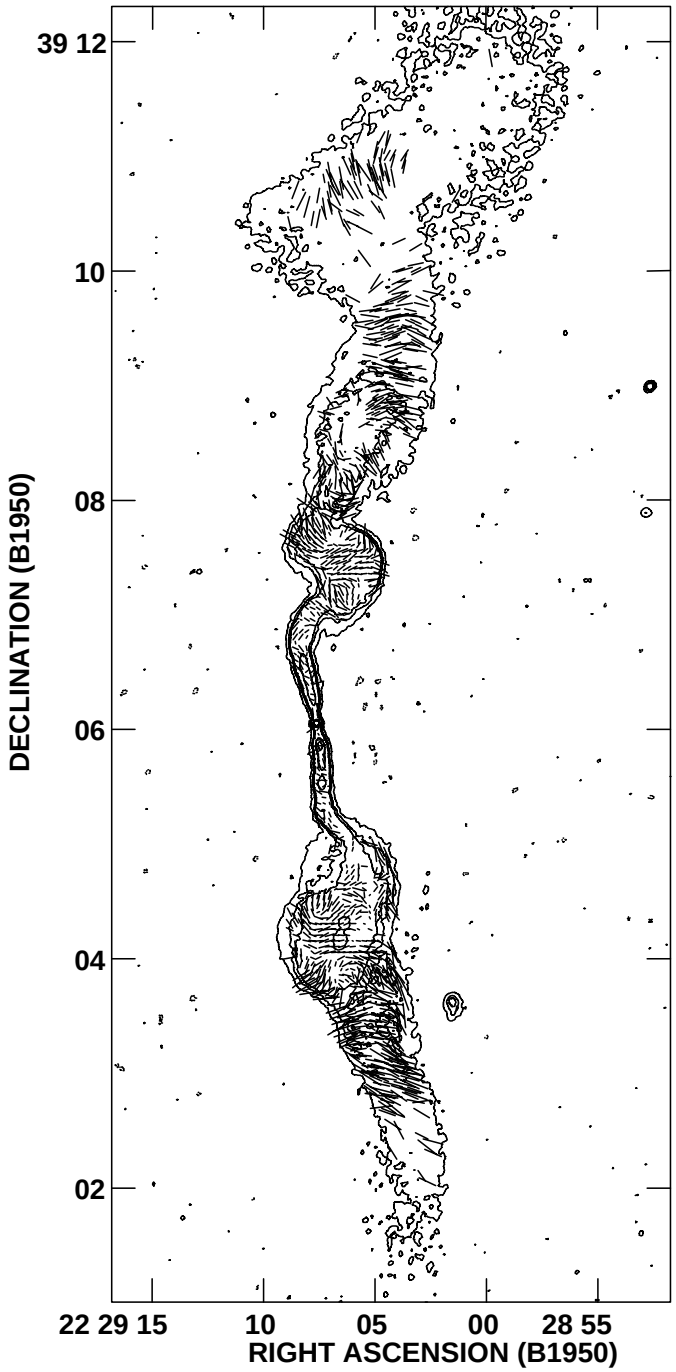

Fig. 10. The 1.485 GHz map, with 2.5″ resolution, showing the polarization vectors (E field, uncorrected for RM). They are proportional in length to the fractional polarization, with 1″ corresponding to 5%. Contour levels are -0.1, 0.1, 0.5, 1, 5, and 10 mJy/beam. The rms noise level in the total intensity map is 0.032 mJy/beam.

the region where the jet magnetic field changes its orientation, from longitudinal to transversal (see Fig. 8).

The brightness is different in the two jets, and is higher, on average, in the southern jet. In both jets, the overall trend of brightness against width is very different from that expected in an adiabatic jet with constant velocity (see Sect. 4.4).

4.2. Core prominence

Assuming that the jets are relativistic at their origin, information on their orientation with respect to the line of sight can be inferred from the comparison between the core radio power and the total radio power, following the approach of Giovannini et al. (1994). This argument is based on the fact that the core radio emission contains a Doppler-boosted relativistic jet, whose strength depends on the jet inclination to the line of sight. Given the existence in radio galaxies of a general correlation between the core power at 5 GHz, P_c, and the total radio power at 408 MHz, P_{tot} (Giovannini et al. 1988):

$$LogP_c = 11.01 + 0.47 LogP_{tot} \quad (3)$$

the expected intrinsic core power can be inferred from the total low frequency radio power, which is not affected by Doppler boosting. The P_c-P_{tot} correlation given in Eq. (3) has been obtained using a large sample of radio galaxies oriented at random angles. Therefore, it gives the apparent (beamed) core radio power for a galaxy at the average orientation of 60°. The Doppler enhancement in a jet of velocity βc and spectral index α, oriented at an angle θ to the line of sight is

$$P(\theta) = P[\Gamma(1 - \beta cos\theta)]^{-(2+\alpha)} \quad (4)$$

where Γ is the Lorentz factor, Γ=(1-β^2)$^{-1/2}$. Therefore, the ratio of the measured core power P_{c-obs} to that inferred from Eq. (3), P_{c-exp}, corresponding to θ=60°, is given by:

$$\frac{P_{c-obs}}{P_{c-exp}} = \left(\frac{1 - \beta cos\theta}{1 - 0.5\beta}\right)^{-(2+\alpha)} \quad (5)$$

and provides an estimate of β and θ.

We derived the ratio of the measured to expected core power using the core flux densities at 5 GHz obtained from the present data, and the total flux density at 408 MHz given in Andernach et al. (1992). A statistical uncertainty of 1 r.m.s was taken into account in the flux density measurements, but the most relevant parameter in the determination of this ratio was the core variability (see Table 2 for the values of core flux densities). We obtained that P_{c-obs}/P_{c-exp} is in the range 0.33-0.45. The corresponding allowed region for the two parameters β and θ, assuming α=0, is presented in Fig. 15. It implies a large velocity of the jet at its beginning, and an angle larger than 75°, between the source major axis and the line of sight.

4.3. Jet sidedness

Independent constraints on β and θ can be obtained from the jet to counter-jet ratio. The relativistic beaming effect on two relativistic symmetrical jets, is to enhance the surface brightness of the approaching beam, and decrease that of the receding one. The observed jet to counter-jet ratio R is given by the formula

$$R = (1 + \beta cos\theta)^q (1 - \beta cos\theta)^{-q} \quad (6)$$

where q = 2+α for an isotropic jet with no preferred magnetic field direction (Pearson & Zensus 1987), and q= 3+2α for a jet

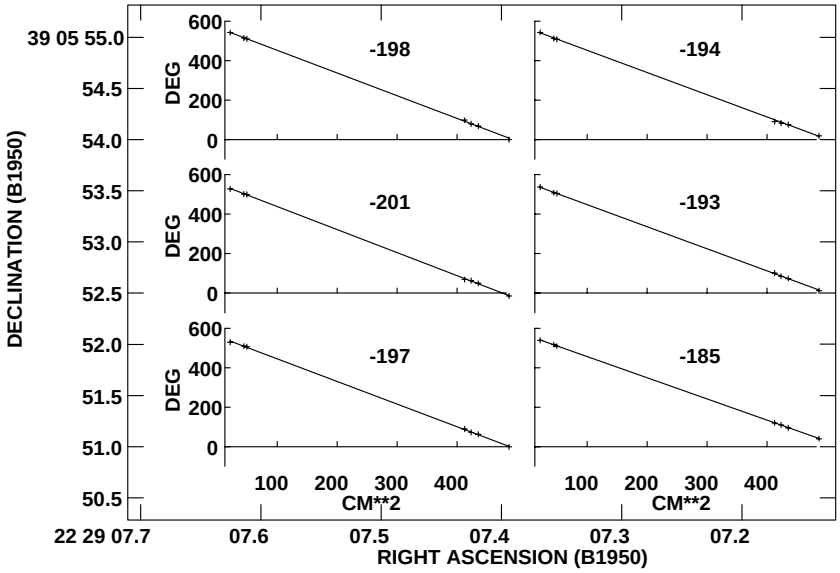

Fig. 11. Samples of the fits to the polarization angle, to obtain the rotation measures. These values refer to the region of the southern jet, at $\sim 8''$ from the nucleus.

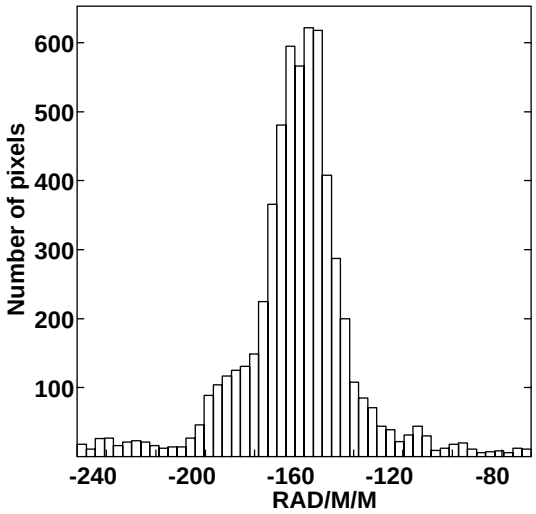

Fig. 12. Histogram of the rotation measure for all significant pixels in the source

with a perfectly ordered longitudinal magnetic field (Begelman 1993). Since the magnetic field is predominantly transversal, and the degree of polarization is low in the region where it is longitudinal (see Sect. 3.3) the formula valid for the isotropic jet is the most appropriate for the present source.

Following Laing (1996), we produced an image of "jet-sidedness", using the 8.4 GHz map at $0.5''$ resolution, and considering the southern jet as the main jet (see Sects. 3.1 and 4.1). Since the two jets show a slightly curved path (see e.g. Fig. 6), the sidedness image is only meaningful in their innermost region, where they are perfectly straight. The image is given in Fig. 16. The average of the values in this map is 1.4, with no distinct trend either along or across the jet. The bright points at the lateral edges could be affected by the slight curvature of the jets.

Fig. 17 gives the run of the jet to the counter-jet ratio along the ridge of maximum brightness. The low values close to the nucleus are in the region where the core has been subtracted, and should not be trusted. This plot cannot be simply interpreted in the framework of the relativistic beaming effects, since it seems to be stronlgy affected by fluctuations related to local enhancements in the jet brightness. The highest value of the jet to counter-jet ratio is $\sim$2.1, and corresponds to the bright spot at about $2''$ from the core, which could be a knot of emission. If instead it is due to relativistic beaming, it implies a value of $\beta cos\theta$=0.14, which leads to a jet velocity of $\approx$ c for a viewing angle of $\approx 82^{\circ}$. The moderate jet asymmetry derived from Figs. 16 and 17 confirms that the source must be at a large angle to the line of sight.

4.4. An adiabatic model for the jets

Information on the jet dynamics has been obtained following the simple approach that the jet is expanding adiabatically, conserving the number of relativistic particles and frozen in magnetic field. Under this assumption, the jet velocity, brightness and opening angle are related. The functional dependence between these parameters has been discussed in the limit of non-relativistic bulk motion with 3-D expansion by Fanti et al. (1982), Bicknell (1984) and Perley et al. (1984). The case of relativistic bulk motion is considered by Baum et al. (1997), who obtain the following relationships:

Predominantly parallel **B** field:

$$I_\nu \propto (\Gamma_j v_j)^{-(2\alpha+3)/3} r_j^{-(10\alpha+9)/3} D^{2+\alpha} \quad (7)$$

Predominantly transverse **B** field:

$$I_\nu \propto (\Gamma_j v_j)^{-(5\alpha+6)/3} r_j^{-(7\alpha+6)/3} D^{2+\alpha} \quad (8)$$

where I_ν is the jet surface brightness, α is the spectral index, v_j and Γ_j are the jet velocity and Lorentz factor, and D is the Doppler factor $D = (\Gamma_j(1 - \beta cos\theta))^{-1}$.

According to these formulae, the widening of the jet at constant velocity results in strong adiabatic losses, which would

cause its dramatic dimming. By deceleration of the advance speed, these adiabatic losses can be balanced and the jet brightness maintained. The apparent brightness of the jet is also affected by relativistic Doppler boosting.

Using the above relationships, we have modeled the jet intrinsic brightness and width as a function of distance, to derive the jet velocity. In this procedure, the input parameters are the orientation of the magnetic field, taken from the from the observations, the initial jet velocity, β_i, and the inclination angle of the jet with the respect to the line of sight, θ, which are both assumed.

The jet observational parameters are well reproduced by the trends given in Fig. 18 (see caption), which correspond to pairs of the initial velocity and inclination angle consistent with the constraints obtained by the core prominence argument. We modeled both the (southern) jet, and the (northern) counter-jet, using the appropriate orientation, and we obtained very similar trends. The important result is that always the jet velocity strongly decreases with distance up to $\sim 10''$ (5 kpc) from the core, and shows almost constant values further out.

The jet/counter-jet ratios derived from the velocity trends displayed in Fig. 18 are plotted in Fig. 17, for a comparison with the observed values (continuous line). The two models with lower initial velocity are more appropriate to reproduce the jet to counter-jet ratios. They imply that the initial peak is mostly due to a local knot, and also the jet asymmetry at $10''$-$13''$ from the core cannot be ascribed to Doppler boosting.

Assuming the orientation of 3C 449 of $\sim 82.5^\circ$ to the line of sight, and the jet velocity running from 0.9c to 0.7c in the inner $5''$-$6''$ (Fig. 18), the Doppler factor is in the range 0.5-0.9. A Doppler factor lower than 1 means that the jets are strongly deboosted and the observed brightness is lower than their intrinsic brightness. This is in agreement with the fact that the innermost jets show very low brightness, and could explain the presence of a "gap" region between the nucleus and the jets in many FR I sources.

We finally note that acceptable fits to the observational jet parameters can be also obtained using values of the initial jet velocity lower than those implied by the core prominence. In particular, it is interesting that starting with β_i=0.5, the jet velocity beyond $10''$ drops to $\beta \sim 0.01$, which would be consistent with the velocity inferred by Hardee et al. (1994) from the observed trajectory of the southern jet, as a result of the orbital motion of the central engine. This case, however, does not account for the innermost low brightness of the jets as due to Doppler de-boosting, and can only be reconciled with the core prominence argument assuming that a strong jet deceleration takes place very close to the nucleus.

Our main conclusion is that the simple adiabatic model provides evidence for a jet deceleration within a few arcsec, i.e. a few kpc, from the nucleus. The strong jet deceleration occurs in the region where the magnetic field changes the orientation, from longitudinal to transversal. A likely mechanism for the jet deceleration is the interaction between the jet and the external medium, i.e. the entrainment of material from the surrounding medium. In particular, the pressure of the gaseous atmosphere

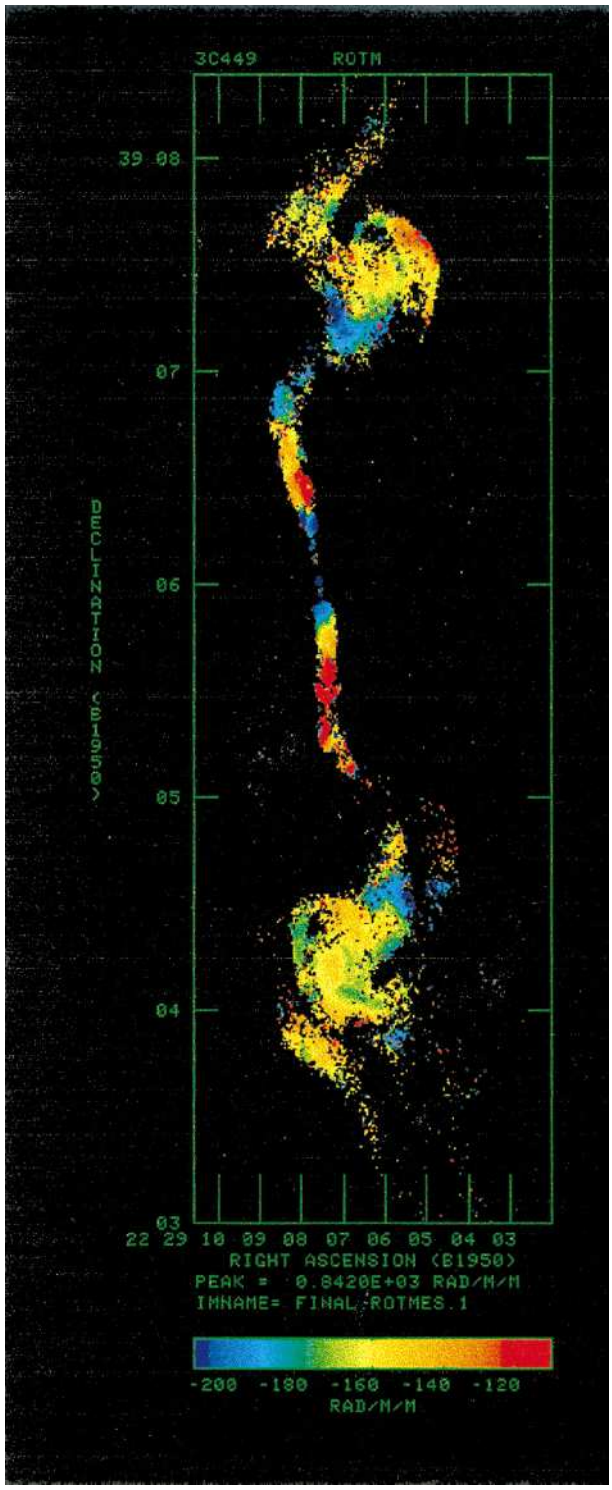

Fig. 13. Map of the rotation measure at $1.25''$ resolution, computed using all 7 frequencies ranging from 1.365 GHz to 8.4 GHz.

associated with the galaxy, would confine the jets and affect the jet dynamics (Bicknell et al. 1990). This behaviour is in agreement with the unified models, and seems to be typical in FR I radio jets, as modeled for 3C 31 by Laing (1996). In the Laing model, the jet consists of a central spine, with higher velocity

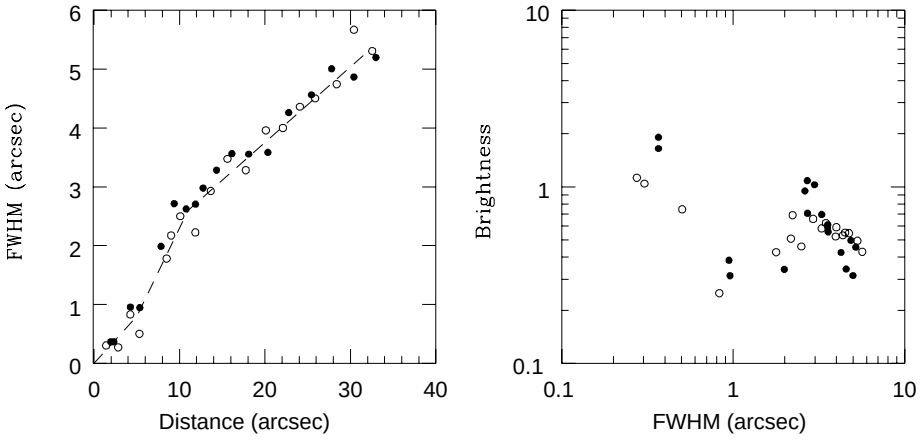

Fig. 14. Plot of the jet deconvolved FWHM versus distance (*left*), and of the jet peak brightness versus FWHM (*right*), with $0.5''$ resolution. Dots and open circles refer to the southern and northern jet, respectively. The dashed line in the left panel represents the best fit to the data in the 3 collimation regimes.

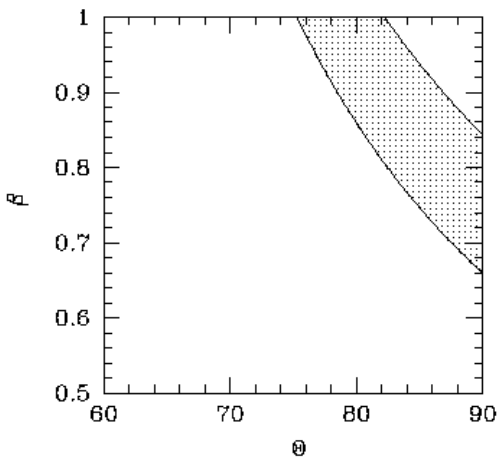

Fig. 15. Allowed region (*shaded*) for the jet velocity and inclination to the line of sight, from the core prominence relative the total flux.

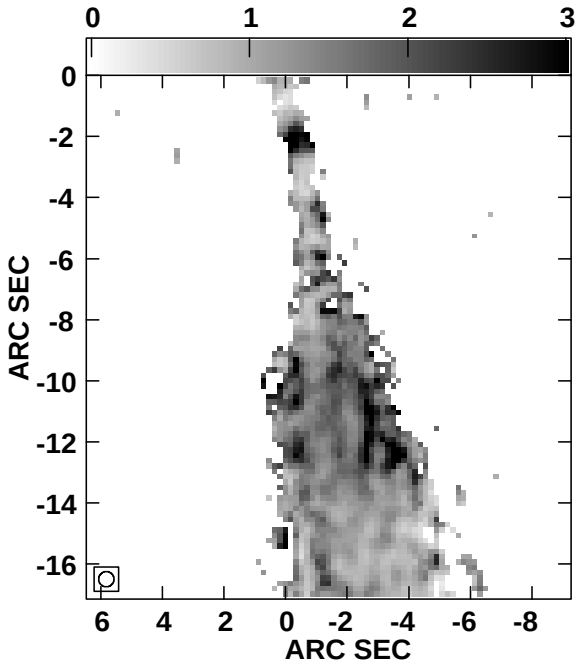

Fig. 16. Map of the jet to counter-jet ratio, computed at 8.4 GHz with $0.5''$ resolution. The coordinate scale is labelled in arcsec relative to the core position

and transverse magnetic field, and a shear-layer with lower velocity and either a longitudinal or a two-dimensional field. We do not detect these two components in the inner jets, either in the sidedness image, or in the structure of the magnetic field. Hardcastle et al. (1997) found a similar problem in 3C 296. In 3C 449, the large orientation angle of the source with respect to the line of sight could make it difficult to distinguish the two components, since the Doppler boosting is not strong enough to significantly enhance the high velocity component with respect to the low velocity one.

4.5. Case of non-relativistic nuclear ejection

The discussion in the above subsections was based on the assumption that the nucleus of 3C 449 ejects highly relativistic jets. Since no VLBI observations are presently available for 3C 449, the emission of the jets at non-relativistic speed in principle cannot be ruled out. An explanation of the structure of 3C 449, assuming that the nucleus ejects a moderately relativstic electron-proton jet with $v_j \simeq 0.4c$, has been provided by Roland et al. (1992). In their scenario, if the mass ejected is large enough and the jet is well collimated, the jet kinetic energy density $\rho_j v_j^2$ (where ρ_j is the jet density) is much greater than the external pressure P_{ext}. This is the case for the innermost region, i.e. within $6''$ from the core, where the jets have low brightness and small opening angle. As the jets open, for a critical radius of the jets, the kinetic energy density becomes comparable to the pressure of the external medium. Here, the jets interact with the outer medium and dissipate their kinetic energy via turbulence. The relativistic electrons are accelerated by the turbulence in the dissipation area, which corresponds to the bright jets up to about $1'$ from the core. Beyond this distance, the dissipation process is finished and the jet velocity becomes smaller or equal to the sound speed of the external medium.

4.6. Spectral behaviour

KR studied the spectral behaviour of 3C 449 over 3 frequencies (0.3, 1.4, and 4.8 GHz), using a new analysis tool, the spec-

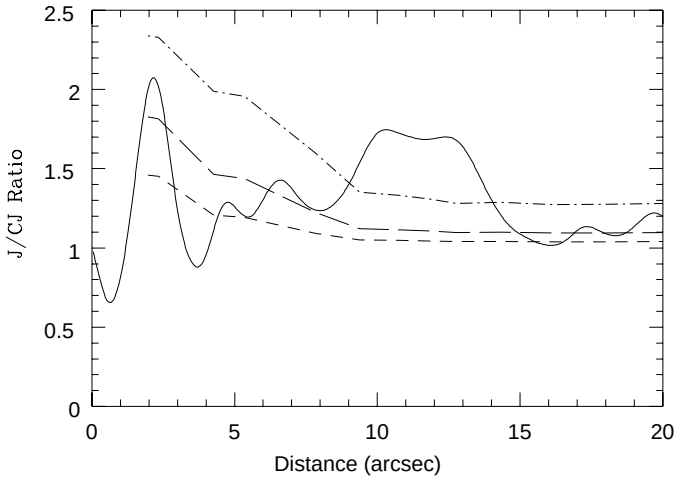

Fig. 17. Brightness ratio of the jet to counter-jet as a function of the distance from the core, along the ridge of source maximum brightness (continuous line). Typical 1σ errors are about 0.06 close to the nucleus, and progressively decrease with distance down to 0.02. The dashed lines correspond to the expected ratios for the jet models given in Fig. 18 (with the same meaning of the line-types).

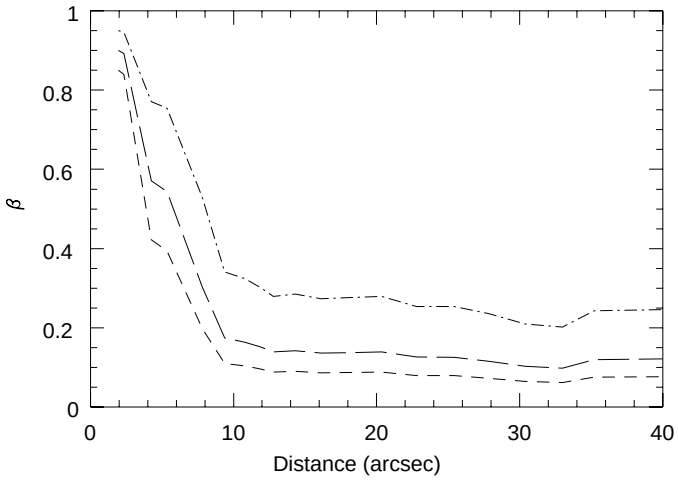

Fig. 18. Trend of β as a function of the distance from the core, in the adiabatic model. The different line-types refer to the following models (consistent with the allowed region of Fig. 15): short-dash: $\theta = 85°$ and $\beta_i = 0.85$; long-dash: $\theta = 82.5°$ and $\beta_i = 0.90$; dot-dash: $\theta = 80°$ and $\beta_i = 0.95$.

tral tomography, which allowed them to isolate the contribution of two different spectral components, the "flat jet", and the "sheath". The flat jet remains fairly well collimated within $2.5'$ from the core, is characterized by a power-law spectrum with $\alpha = 0.53 \pm 0.01$, and shows little steepening with distance from the core. The second component, the "sheath", appears beyond $1'$ from the core, on both sides of the jet, and is responsible for most of the observed widening. The spectrum of the "sheath" is steeper than that of the "flat jet", and has a range of spectral indices with typical values at $2.5'$ from the core of 0.57 ± 0.02 in the north, and 0.69 ± 0.02 in the south. We refer the reader to the paper by KR for the interpretation of the two jet components.

Our spectrum between 4.985 GHz and 8.4 GHz (Fig. 7) reveals the existence of a spectral asymmetry between the northern and southern inner lobes. A similar asymmetry is found by KR in the sheath. For the flat jet, i.e. within $1'$ from the core, we obtain $\alpha_5^{8.4} = 0.58 \pm 0.03$, which is consistent with the value of KR, and implies that the flat jet has a power law spectrum extending up to 8.4 GHz. In the northern inner lobe (N2), we find an average value $\alpha_5^{8.4} = 0.57 \pm 0.03$, and we do not distinguish between the two components found by KR. In the southern inner lobe (S2), we separate the flat jet with spectral index $\alpha_5^{8.4} = 0.74 \pm 0.03$, from the surrounding region which reaches values up to $\alpha_5^{8.4} \sim 0.9$. A possibility is that the apparent jet in the southern inner lobe (S2) is a case where the jet enters the lobe, but does not diffuse directly in it. Rather, the jet's momentum is sufficient to carry it through the lobe, as a distinct entity. As the jet moves around, perhaps due to tidal forces on the nucleus, the orientation of the jet's exhaust into the lobe could change, permitting the lobe to be expanded from a different input angle. Our results indicate steeper spectra than those obtained by KR. The implication is that both jet components show a spectral steepening at a frequency beyond 5 GHz. It is clear from the spectral behaviour, that reacceleration processes are much more efficient in the northern region. This could cause the larger total extent of the northern half of the source, with respect to the southern one.

4.7. Interpretation of RM data

The Faraday rotation of extragalactic radio sources can originate inside the radio-emitting regions if sufficient thermal material is mixed with the synchrotron radiating plasma, or could be of external origin if magnetic field and thermal gas are present along the line of sight. The interpretation of polarization data has been summarized by Laing (1984): if the polarization angle obeys a λ^2 law, and the rotation persists over an angle larger than $\pi/2$, the Faraday rotation is due to a foreground screen.

The values of RM are generally small, ranging from -50 to +50 rad m^{-2}, with respect to the expected foreground rotation of our Galaxy (-162 rad m^{-2}). A significant contribution to the Galactic value probably originates from the Galactic feature crossing the region south of the galaxy associated with 3C 449 (Andernach et al. 1992). This feature seems to affect in the same way the rotation measure of all the region mapped by us, with no difference between the northern and southern region.

The good λ^2 fits of the polarization angle (Fig. 11) are in favour of an external origin for the RM. The foreground screen seems to be fully resolved, since there is no significant difference between RM images at different resolutions, and no strong depolarization is present at low frequency. The moderate depolarization of the jets (Sect. 3.3) could originate within the jets, from the likely entrainment.

A likely external Faraday screen is the intergalactic medium associated with the galaxy group around 3C 449. The fact that the RM structure is very similar in the N and S lobes is consistent with the orientation of this radio galaxy in the plane of the sky. From the analysis of X-ray data, Hardcastle et al. (1998) derived

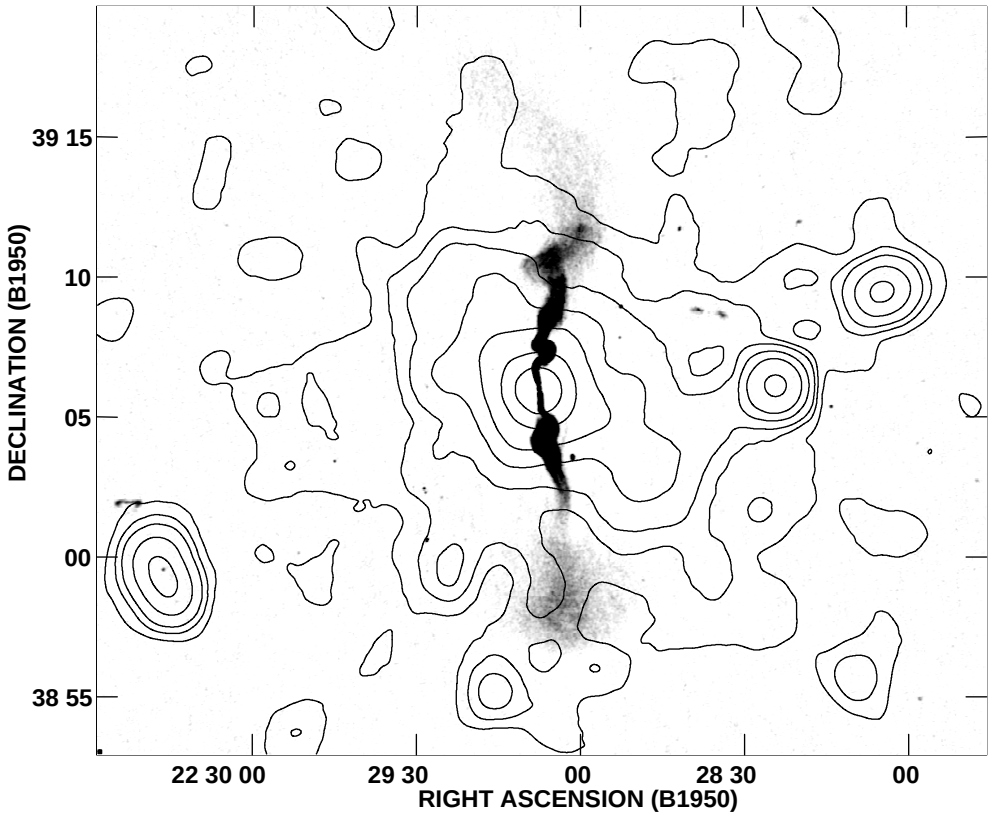

Fig. 19. Overlay of the grey-scale radio image at 1.365 GHz, with 5″ resolution, onto contours of the X-ray image obtained with the ROSAT PSPC. Contours ar drawn at 14%, 18%, 23%, 30%, 40%, 60%, and 80% of the X-ray peak.

a central gas density of 4.6×10^{-3} cm^{-3}, and a core radius of the gas distribution of 35″(18 kpc). Significant deviations of the RM from the Galactic value are present in the jets up to 1′-1.1′ from the core, i.e. about 2 core radii. A cluster magnetic field of ∼0.7-0.9 μG, ordered on scales of ∼5 kpc is necessary to produce the observed values of RM.

A remarkable feature in the map of the RM is the large symmetry in the innermost jets, within ∼15″ from the core, where the RM assumes values more negative than the Galactic value, with a possible trend that the lowest values are seen closer to the nucleus. From the surface brightness profile given by De Juan et al. (1994), the galaxy brightness at a radius of about 15″ decreases by about a factor of 100 with respect to the peak value (see also Fig. 2). A plausible scenario is that the gaseous atmosphere associated with the galaxy, and influencing the jet dynamics, is responsible for the rotation measure and for the low fractional polarization of the innermost jets. To account for the observational data, we have to assume that the magnetic field associated to the galaxy is highly tangled.

4.8. Comparison with the X-ray emission

In Fig. 19 the radio image of 3C 449 is overlaid to the ROSAT image, obtained with a PSPC pointing observation, with an exposure of 9500 sec (Hardcastle et al. 1998). The data were retrieved from the public ROSAT archive. The image was produced by binning the photon event table in pixels of 15″, and by smoothing the map with a gaussian of σ = 45″. As discussed by Hardcastle et al. (1998), the large scale structure of 3C 449 is determined by the distribution of the hot intergalactic plasma. The X-ray gas is not spherically symmetric, and the low brightness radio emission is anti-coincident with the X-ray filaments. The large-scale radio emission avoids the regions of high X-ray brightness, and the radio streamers flow where the X-ray gas is less dense.

This effect could be due to the buoyancy of the radio plasma in a pressure gradient. The sharp bend in region N4 seems to be related to the existence of a subclump in the X-ray gas.

5. Conclusions

We have presented sensitive multifrequency radio maps of the giant radio galaxy 3C 449, and studied its properties in total and polarized intensity. We have mapped the source up to a total extent of 20′. Our conclusions are as follows.

1) The source shows a slightly variable unresolved core, two opposite jets, and very extended lobes characterized by plumes and wiggles. It is highly polarized at all frequencies from 1.4 GHz to 8.4 GHz.

2) The two jets are misaligned by ∼11°, but are fairly symmetrical at the resolution of 5″ for about 1′ from the radio core. They both bend westward at ∼45″ from the core, and at ∼ 1′ they merge into the inner lobes, beyond which they follow a sort of helical structure. At the highest resolution, the jets show some asymmetry, with the southern jet being brighter on average than the northern one. No gap of radio emission is found close to the nucleus. The two jets are not perpendicular to the dust lane detected in the nucleus of the parent galaxy of 3C 449.

3) The southern and northern jets show similar collimation properties, with a constant expansion rate at the beginning, a rapid expansion between 6″ and 10″ from the core, and a recollimation further out. The magnetic field direction is parallel to the jet axis in the first 8″, and then becomes transversal.

4) From the prominence of the core power over the total radio power, we infer that the jets are relativistic at their beginning and the source is oriented at an angle larger than 75° to the line of sight. This is confirmed by the level of symmetry/asymmetry found in the brightness ratios of jet to counter-jet.

5) From the application of the simple adiabatic model to the jets, evidence of a strong jet deceleration within 10″ (5 kpc) from the nucleus is found. A satisfactory fit to the data is found assuming an initial jet velocity of 0.9c, and a jet inclination to the line of sight of 82.5°. The trend of jet velocity obtained in this way is consistent with the jet to counter-jet ratios, and with the low brightness of the innermost jets, as due to Doppler deboosting. The strong jet deceleration occurs in the region where the magnetic field changes the orientation, from longitudinal to transversal. A likely mechanism for the jet deceleration is the entrainment of material from the surrounding medium.

6) The spectrum between 5 GHz and 8.4 GHz in the northern inner lobe is flatter than in the southern inner lobe. Therefore, reacceleration processes seem to be much more efficient in the northern than in the southern region. This could cause the larger total extent of the northern half of the source, with respect to the southern one.

7) The polarization angles are well fitted by a λ^2 law, which persists over about 500° and is indication of an external origin for the RM. Values of RM are within ± 50 rad m^{-2} of the Galactic value. They are likely to originate in the intergalactic medium associated with the galaxy group of 3C 449, but also the interstellar medium of the galaxy itself seems to contribute to the RM, in the innermost jet region.

Acknowledgements. We thank Dr. Greg Taylor for providing the code for the evaluation of the rotation measure with 7 frequencies. Thanks are due to Dr. Isabella Gioia for the optical image of the region of the arc-like feature, and for comments on the manuscript. We acknowledge helpful discussions with Drs. José Luis Gomez and Roberto Fanti. We thank our referee, Dr. Jacques Roland, for discussions which were helpful in illuminating fine points of the two-fluid model.

H.A. benefitted from financial support by CONACYT (Mexico; Cátedra Patrimonial, ref 950093).

The National Radio Astronomy Observatory is operated by Associated Universities, Inc., under contract with the National Science Foundation.

References

Andernach H., Feretti L., Giovannini G., et al., 1992, A&AS 93, 331
Balcells M., Morganti R., Oosterloo T., Pèrez-Fournon I., Gonzalez-Serrano J.I., 1995, A&A 302, 665
Baum S.A., O'Dea C.P., Giovannini G., et al., 1997, ApJ 483, 178
Begelman M.C. 1993, In: Röser H.-J., Meisenheimer K. (eds.) Jets in Extragalactic Radio Sources. Springer-Verlag, p. 145
Bicknell G.V., 1984, ApJ 286, 68
Bicknell G.V., de Ruiter H., Fanti R., Morganti R., Parma P., 1990, ApJ 354, 98
Biretta J., 1996, In: Hardee P.E., Bridle A.H., Zensus J.A. (eds.) Energy Transport in Radio Galaxies and Quasars. ASP Conference Series n. 100, p. 187
Bridle A.H., Perley R.A., 1984, ARA&A 22, 319
Butcher H.R., van Breugel W., Miley G.K., 1980, ApJ 235, 749
Capetti A., Macchetto F., Sparks W.B., Miley G.K., 1994, A&A 289, 61
Capetti A., Celotti A., 1998, MNRAS, submitted
Carilli C.L., Barthel N., Diamond P., 1994, AJ 108, 64
De Juan L., Colina L., Pérez-Fournon I., 1994, ApJS 91, 507
Fanaroff B.L., Riley J.M., 1974, MNRAS 167, 31P
Fanti R., Lari C., Parma P., et al., 1982, A&A 110, 169
Giovannini G., Feretti L., Gregorini L., Parma P., 1988, A&A 199, 73
Giovannini G., Feretti L., Venturi T., et al., 1994, ApJ 435, 116
Giovannini G., Cotton W.D., Feretti L., Lara, L., Venturi, T., Marcaide, J.M., 1995, In: Cohen M.H., Kellermann K.I. (eds.) Quasars and Active Galactic Nuclei: High Resolution Imaging. Proc. Nat. Acad. Sci. USA Vol. 92, Number 5, p. 11356
Hardcastle M.J., Alexander P., Pooley G.G., Riley J.M, 1997, MNRAS 288, L1
Hardcastle M.J., Worral D.M, Birkinshaw M., 1998, MNRAS 296, 1098
Hardee P.E., Cooper M.A., Clarke D.A., 1994, ApJ 424, 126
Katz-Stone D.M., Rudnick L., 1997, ApJ 488, 146 (KR)
Killeen N.E.B., Bicknell G.V., Ekers R.D., 1986, ApJ 302, 306
Laing R.A., 1984, In: Bridle A.H., Eilek J.A. (eds.) Physics of Energy Transport in Extragalactic Radio Sources. NRAO Workshop n. 9, p. 90
Laing R.A., 1996, In: Hardee P.E., Bridle A.H., Zensus J.A. (eds.) Energy Transport in Radio Galaxies and Quasars. ASP Conference Series n. 100, p. 241
Parma P., De Ruiter H.R., Fanti R., Laing R., 1994, In: Bicknell G.V., Dopita M.A., Quinn P.J. (eds.) The Physics of Active Galaxies. ASP Conference Series Vol. 54, p. 241
Pearson T.J., Zensus J.A., 1987, In: Zensus J.A., Pearson T.J. (eds.) Superluminal Radio Sources. Cambridge Univ. Press, p. 1
Pelletier G., Roland J., 1989, A&A 224, 24
Pelletier G., Roland J., 1990, In: Zensus J.A., Pearson T.J. (eds.) Parsec-scale Radio Jets. Cambridge University Press, p. 323
Pelletier G., Sol H., 1992, MNRAS 254, 635
Perley R.A., Willis A.G., Scott J.S., 1979, Nat 281, 437
Perley R.A., Bridle A.H., Willis A.G., 1984, ApJS 54, 291
Roland J., Lehoucq R., Pelletier G., 1992, In: Roland J., Sol H., Pelletier G. (eds.) Extragalactic Radio Sources: From Beams Beams to Jets. Cambridge Univ. Press, p. 294
Sol H., Pelletier G., Asseo E., 1989, MNRAS 237, 411
Tingay S.J., Jauncey D.L., Reynolds J.E., et al., 1998, ApJ 115, 960
Urry C.M., Padovani P., 1995, PASP 107, 803
Wardle J.F.C., Kronberg P.P., 1974, ApJ 249, 255